Heliyon

Dual phototransformation of the pollutants methyl orange and Cr (VI) using phthalocyanine-cobalt ferrite based magnetic nanocomposites

Sivuyisiwe Mapukata, Olawale L. Osifeko, Tebello Nyokong[*]

Centre for Nanotechnology Innovation, Department of Chemistry, Rhodes University, Grahamstown 6140, South Africa

[*] Corresponding author.

E-mail address: t.nyokong@ru.ac.za (T. Nyokong).

Abstract

Bifunctional nanocomposites based on zinc phthalocyanines and glutathione capped $CoFe_2O_4$ magnetic nanoparticles (GSH-$CoFe_2O_4$ MNPs) are applied in a binary system wherein simultaneous photooxidation of methyl orange (MO) and photoreduction of Cr (VI) are conducted. The photoactivity of two zinc Pcs with different functional moieties are compared based on their interactions with GSH-$CoFe_2O_4$ MNPs. Conjugation of the Pcs to the GSH-$CoFe_2O_4$ MNPs not only enhanced their singlet oxygen production but also their photocatalytic activity in both photooxidation and photoreduction experiments. Using electron paramagnetic resonance (EPR) spectroscopy, the Pc-MNP conjugates reported herein were found to exhibit superparamagnetic behaviour, giving the advantage of easy separation using an external magnetic field post application, an attractive attribute for heterogeneous catalysis. The catalysts reported herein are therefore good candidates as catalysts for real life water purification analyses as they facilitate the treatment of both organic and inorganic water pollutants.

1. Introduction

Phthalocyanines (Pcs) have been extensively studied in applications such as electrochemical sensors, liquid crystals, dye-sensitized solar cells, nonlinear optics and photodynamic therapy [1, 2, 3, 4, 5, 6]. Due to their excellent visible/near infrared absorption, high chemical and thermal stability and the ability of generate singlet oxygen, Pcs have also been reported as good photocatalysts for the degradation of organic dyes [7, 8]. Photocatalysis has been proposed as an effective advanced oxidation process (AOP) for the degradation of organic pollutants. Photocatalysis may completely degrade pollutants without giving rise to undesired by-products, which may be even more toxic than the parent compound. However, photocatalysis using Pcs has mainly been used for organic pollutants and this work presents the use of Pcs for photocatalysis of an inorganic pollutant, Cr(VI), in the presence of ferrites.

Ferrites are also commonly used photocatalysts, they have band gaps of approximately 2 eV which in turn enable them to absorb visible light [9, 10]. They have been used in various applications including photocatalysis, as multiferroic materials and magnetic labelling of biological systems [10, 11, 12, 13].

In this work, we link the two photocatalysts (Pcs and ferrites) for improved photocatalytic activity by a synergistic effect. Conjugates of gluthathione capped cobalt ferrite magnetic nanoparticles (GSH-CoFe$_2$O$_4$ MNPs) with 2(3),9(10),16(17),23(24)-tetrakis-(4'-(4'-6'-diaminopyrimidin-2'-ylthio))) phthalocyaninato zinc (II) (complex **1**) and zinc tetraaminophenoxy phthalocyanine (complex **2**) are synthesised. They are then employed for the photodegradation of methyl orange (MO) and the photoreduction of hexavalent chromium, common water pollutants.

Complexes **1** and **2** are conjugated to mixed metal MNPs which show more catalytic activity compared to the corresponding single component metal oxides [14]. Glutathione was used for functionalising the CoFe$_2$O$_4$ MNPs because in addition to it having the appropriate terminal groups for amide bond formation with the Pc complexes, glutathione has itself been reported to possess photoreduction ability for Cr (VI) [15, 16]. Apart from our recent report [17], there are no reports on linking Pcs to bimetallic MNPs. The conjugates reported herein are employed as dual photocatalysts for both photoreduction of Cr (VI) and photodegradation of MO. This is the first time that Pc-MNP conjugates are employed as dual photocatalysts for both organic and inorganic species using the same photocatalyst.

The reduction of Cr (VI) to Cr (III) is often accelerated in the presence of sacrificial donors such as 4-chlorophenol which prevent the re-oxidation of Cr (III) to Cr (VI). Cr (III) is significantly less toxic than Cr (VI) and is readily removable by alkaline precipitation [18]. In this work, in addition to studying the photodegradation of MO, we use MO as a sacrificial electron donor during the photoreduction of Cr (VI). This is because the hydroxyl radicals (·OH) generated during the photolysis may oxidize Cr (III) back to Cr (VI) [19]. In the presence of MO however, the Cr (III) to Cr (VI) oxidation is suppressed since MO acts as a sacrificial molecule which will react preferentially with the ·OH.

Complex **1** has eight amine groups while complex **2** has four and therefore a comparative study on the effect of the number of amine groups on the photocatalytic behaviour will be examined. The presence of the $CoFe_2O_4$ MNPs in the photocatalysts gives the advantage of magnetic regeneration of the catalyst and hence reusability. In addition, the MNPs also encourage intersystem crossing (ISC) to the triplet state of the Pc, through the heavy atom effect of the metals contained in the MNPs. This enhances the singlet oxygen generating ability of the Pc [7, 8], which is fundamental for their photocatalytic efficiency.

In this work nanocomposites of Pcs and bimetallic $CoFe_2O_4$ MNPs will for the first time be used to facilitate both photoreduction and photodegradation, using Cr (VI) and MO as models, respectively. MO is a synthetic azo (-N=N-) dye that is commonly used in textiles and paper industries [20]. Cr (VI) on the other hand is also used in textiles, tannery industries as well as fertilizers, amongst others [21]. Both of Cr (VI) and MO are toxic pollutants, hence the need of finding means of degrading or transforming them [22, 23].

## 2. Experimental

2.1. Materials

Dimethylsulphoxide (DMSO), dimethylformamide (DMF), Zn phthalocyanine (ZnPc), Na_2HPO_4 and KH_2PO_4 were obtained from SAARChem. N,N-dicyclohexylcarbodiimide (DCC), 1,3-diphenylisobenzofuran (DPBF), methyl orange (MO), chromium (VI) oxide, reduced glutathione (GSH) and iron (III) chloride hexahydrate were purchased from Sigma–Aldrich. Cobalt (II) chloride hexahydrate was purchased from UniLab. All other reagents and solvents were obtained from commercial suppliers and used as received. Aqueous solutions were prepared using millipore water from Milli-Q Water Systems and adjusted to a pH of 2.75 with phosphoric acid from Minema Chemicals. 2(3),9(10), 16(17),23(24)-Tetrakis-(4'-(4'-6'-diaminopyrimidin-2'-ylthio)))phthalocyaninato zinc (II) (**1**) [24] and zinc tetraaminophenoxy phthalocyanine (**2**) [25,26] were synthesized according to literature methods.

2.2. Methods

2.2.1. Synthesis of magnetic nanoparticles (MNPs)

2.2.1.1. Synthesis of bare CoFe$_2$O$_4$ MNPs (Fig. 1A)

The MNPs were prepared by the conventional co-precipitation method as reported before [27] with slight modifications as follows: iron (III) chloride hexahydrate (25 mL, 0.4 M) and cobalt (II) chloride hexahydrate (25 ml, 0.2 M) were mixed together. Ammonium hydroxide (25%) was added dropwise to the solution until a pH of 10−12 was reached. The solution was then heated to 85 °C for 1 h and then cooled to room temperature. The precipitated nanoparticles were then retrieved by magnetic decantation, washed with water
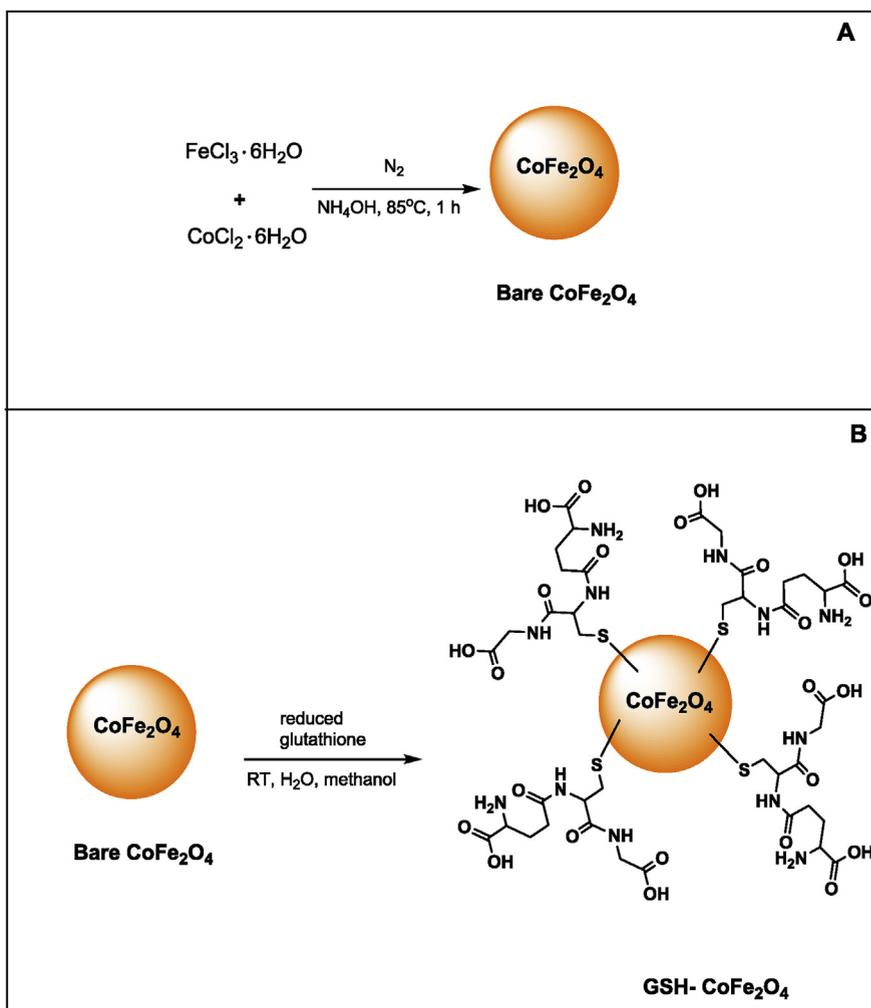
Fig. 1. (A) Synthesis of bare CoFe$_2$O$_4$ MNPs and (B) functionalization of CoFe$_2$O$_4$ MNPs with GSH.

three times and then dried overnight under vacuum to form the bare $CoFe_2O_4$ MNPs.

2.2.1.2. Functionalisation of the bare CoFe₂O₄ MNPs to form GSH-CoFe₂O₄ (Fig. 1B)

The bare $CoFe_2O_4$ MNPs were modified by anchoring of glutathione (GSH) onto the surface of the ferrite as reported before [28] with slight modifications as follows: bare $CoFe_2O_4$ MNPs (0.5 g) were dispersed in a solvent mixture of water (15 mL) and methanol (5 mL) and sonicated for 15 min. Reduced glutathione was then dissolved in water (15 mL) and added to the solvent mixture drop-wise followed by sonication for a further 2 h. The resultant GSH-$CoFe_2O_4$ MNPs were then magnetically separated washed with methanol and dried under vacuum overnight.

2.2.2. Conjugation of complexes 1 and 2 to GSH-CoFe₂O₄ forming CoFe₂O₄-1 and CoFe₂O₄-2 (Figs. 2 and 3)

Conjugation of the GSH-$CoFe_2O_4$ MNPs with complexes **1** (Fig. 2) and **2** (Fig. 3) was done as reported in literature [29] as follows: in two separate round bottomed flasks, a mixture of GSH-$CoFe_2O_4$ MNPs (0.1 g) and DCC (0.02 g, 0.097 mmol) in DMF (4 mL) was added, followed by stirring at room temperature for 48 h. Complexes **1** and **2** (0.10 g, $\sim$ 0.088 mmol) were then added to the mixtures and stirring was continued for another 48 h. The conjugates were collected and purified with acetone, methanol, and ethanol in succession. The resulting products (CoFe$_2$O$_4$-**1** and CoFe$_2$O$_4$-**2**) were dried under vacuum overnight.

2.2.3. Photophysical parameters

Fluorescence (Φ_F), triplet (Φ_T), and singlet oxygen (Φ_Δ) quantum yields were determined in DMSO using comparative methods described before in literatures [30, 31, 32, 33]. Unsubstituted ZnPc in DMSO was used as a standard with $\Phi_F = 0.20$ [31], $\Phi_\Delta = 0.67$ [33] (using DPBF as a singlet oxygen quencher), and $\Phi_T = 0.65$ [32]. The solutions for triplet state studies were de-aerated with argon for 15 min before measurements.

2.3. Instrumentation

UV−Vis absorption spectra were measured at room temperature on a Shimadzu UV-2550 spectrophotometer using a 1 cm pathlength cuvette in solution. Fluorescence emission and excitation spectra were obtained on a Varian Eclipse spectrofluorimeter using a 1 cm pathlength quartz cuvette. IR spectra were recorded on a Perkin-Elmer Spectrum 100 ATR FT-IR spectrometer.
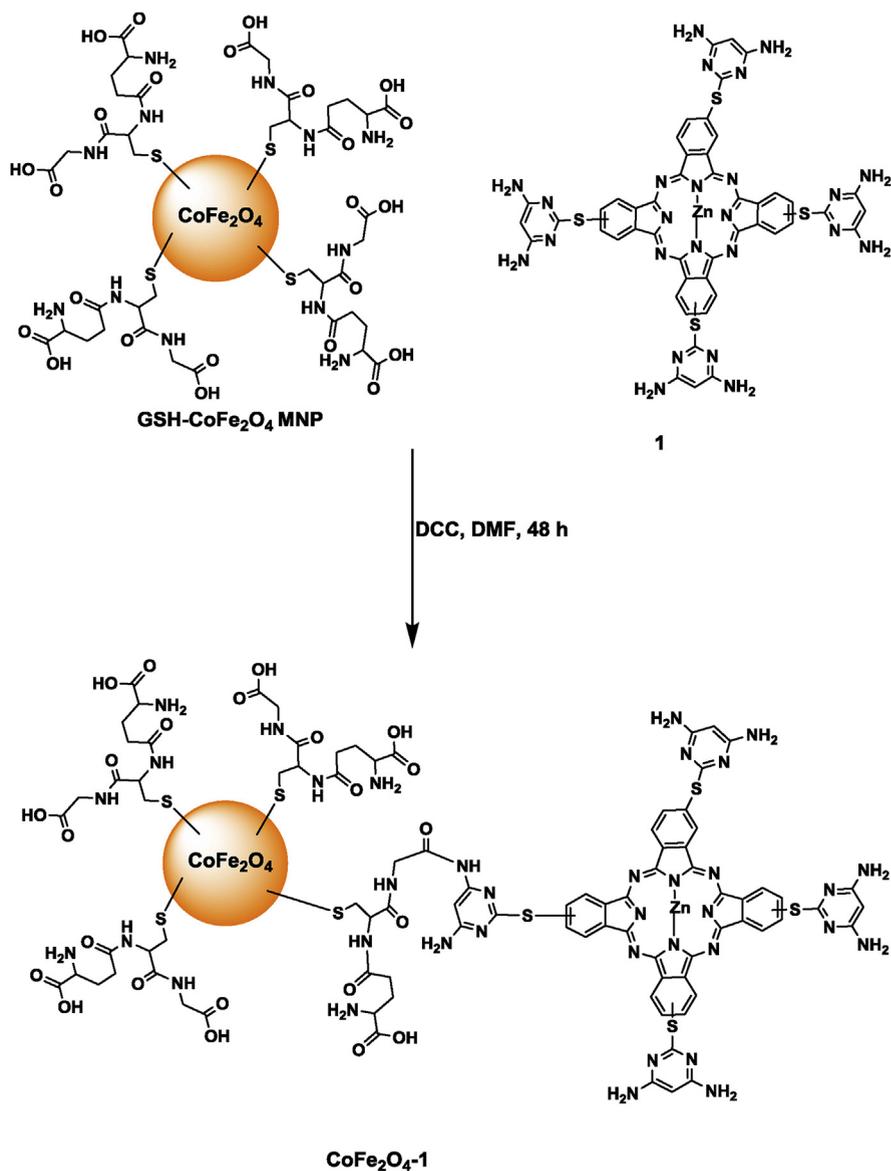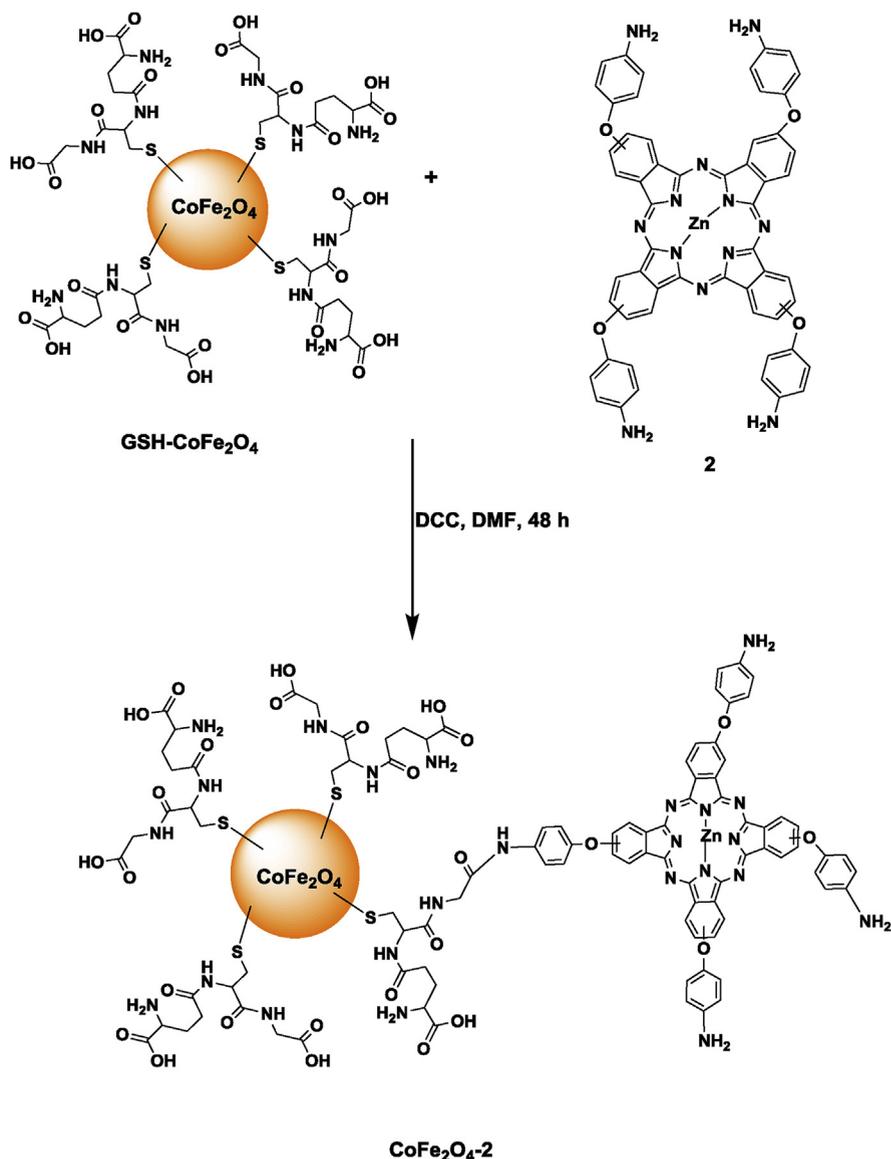
Fig. 2. Conjugation of GSH-CoFe$_2$O$_4$ MNPs to complex **1**.

Fluorescence decay times were measured using a time correlated single photon counting (TCSPC) setup (FluoTime 300, Picoquant GmbH). The excitation source was a diode laser (LDH-P-670 driven by PDL 800-B, 670 nm, 20 MHz repetition rate, 44 ps pulse width, Pico quant GmbH). Triplet quantum yields were determined using laser flash photolysis system. The excitation pulses were produced using a tunable laser system consisting of a Nd:YAG laser (355 nm, 135 mJ/4−6 ns) pumping an optical parametric oscillator (OPO, 30 mJ/3−5 ns) with a wavelength range of 420−2300 nm (NT-342B, Ekspla) as described before [34].

Fig. 3. Conjugation of GSH-CoFe$_2$O$_4$ MNPs to complex **2**.

Energy dispersive X-ray spectroscopy (EDX) was done on an INCA PENTA FET coupled to the VAGA TESCAM using 20 kV accelerating voltage. Dynamic light scattering (DLS) experiments were done on a Malvern Zetasizer Nanoseries, Nano-ZS90. X-ray powder diffraction (XRD) patterns were recorded on a Bruker D8 Discover equipped with a Lynx Eye Detector, using Cu-Kα radiation (λ = 1.5405 A, nickel filter). Details have been reported before [8].

X-ray photoelectron spectroscopy (XPS) analysis was done using an AXIS Ultra DLD, with Al (monochromatic) anode equipped with a charge neutraliser, supplied by Kratos Analytical. The following parameters were used: the emission was 10 mA, the anode (HT) was 15 kV and the operating pressure below 5×10^{-9} torr. A hybrid

lens was used and resolution to acquire scans was at 160 eV pass energy in slot mode. The centre used for the scans was at 520 eV with a width of 1205 eV, steps at 1 eV and dwell time at 100 ms. The high resolution scans were acquired using 80 eV pass energy in slot mode.

Electron paramagnetic resonance (EPR) measurements were carried out using a Bruker EMX Plus EPR spectrometer, model number: EMP-9.5/12B/P. EPR settings were: the microwave power was 0.632 mW, frequency 9.714 GHz, resolution 2048 points, and centre field 3460 G and 100 G for the sweep width. The position of resonance of a paramagnet is defined by the *g*-factor and it was calculated using Eq. (1):

$$g = \frac{h\upsilon}{H\beta} \tag{1}$$

where h is the Planck's constant, υ is the frequency of the microwave, H is the magnetic field occurring, and β is the Bohr magneton [35].

Measurement of singlet oxygen quantum yields as well as photocatalytic reactions for MO and Cr (VI) were carried out using irradiation from a halogen lamp (300 W), 600 nm glass (Schott) and water were used to filter off ultra-violet and far infrared radiation, respectively, as described before [36]. Light intensities were measured with a POWER MAX 5100 (Molelectron detector incorporated) power meter and were found to be 3.8×10^{16} photons/cm^2 s for singlet oxygen studies.

3. Results and discussion

3.1. Synthesis and characterization of the conjugates

GSH-CoFe$_2$O$_4$ MNPs were synthesized as reported before [27, 28] with modifications (Fig. 1). Various methods have been reported on the synthesis of cobalt ferrite MNPs such as the sonochemical method, mechanochemical method, co-precipitation and the micro-emulsion procedure [37, 38, 39, 40, 41]. In this work the co-precipitation method is implemented due the fact that, relative to other known techniques, small particle sizes can be obtained at low temperatures [40].

Following activation of the carboxylic acid groups of the GSH-CoFe$_2$O$_4$ MNPs with DCC, they were linked via amide bond formation with complexes **1** and **2** forming CoFe$_2$O$_4$-**1** and CoFe$_2$O$_4$-**2** respectively (Figs. 2 and 3). Since Pcs have sizes of about ~1 nm and the GSH-CoFe$_2$O$_4$ MNP have an average size of 10.08 nm (from DLS measurements below), it is unlikely for more than one MNP to be attached to the Pc, but it is possible for more than one Pc to link to the MNP. The number of Pc molecules bonded to the GSH-CoFe$_2$O$_4$ MNPs were determined following literature methods, but using absorption instead of fluorescence [42]. This involves comparing the Q band absorbance intensity of the Pc in the conjugate with that of the initial Pc before the conjugation. The ratio of the Pcs:MNPs in

Table 1. Photophysicochemical data of complexes **1** and **2** and their respective conjugates ($CoFe_2O_4$-**1** and $CoFe_2O_4$-**2**) in DMSO.

Complexes	Ratio Pc/MNPs	DLS size (nm)[a]	λ_{abs} (nm)	Φ_F	τ_F (ns)	Φ_T	τ_T (µs)	Φ_Δ
1	-	-	689[b]	0.11[b]	2.53[b]	0.83[b]	351[b]	0.30[b]
$CoFe_2O_4$-**1**	5:1	14.10	689	0.058	2.29	0.88	355	0.65
2	-	-	686[c]	0.060[c]	2.79[c]	0.51[c]	315[c]	0.38[c]
$CoFe_2O_4$-**2**	8:1	16.95	686	<0.010	2.20	0.85	256	0.62

[a] DLS size for GSH- $CoFe_2O_4$ MNPs alone = 10.08 nm.

[b] values from reference 24.

[c] values from reference 26.

$CoFe_2O_4$-**1** and $CoFe_2O_4$-**2** were found to be 5:1 and 8:1 respectively, Table 1, showing that more molecules of complex **2** are loaded onto the MNPs than there are of complex **1**.

The UV−vis spectra of complex **1** and $CoFe_2O_4$-**1** are shown in Fig. 4A and those of complex **2** and $CoFe_2O_4$-**2** are shown in Fig. 4B. The narrow Q bands of complexes **1** and **2** confirm their monomeric behaviour. No shifts were observed in the Q bands of both Pcs after conjugation (Table 1).

Transmission electron microscopy (TEM) was employed so as to obtain the morphology and dispersion of the MNPs and their respective conjugates. The images (Fig. 5) reveal that the GSH-$CoFe_2O_4$ MNPs and $CoFe_2O_4$-**1** have a predominantly spherical morphology. Due to the superparamagnetic nature of the MNPs however, the TEM images also show that the GSH-$CoFe_2O_4$ MNPs are aggregated and even more so when conjugated to the Pcs ($CoFe_2O_4$-**1** used as an example). The aggregates appear as big clusters of predominantly spheres in the images with some rods also observed. The aggregation is possibly due to the π-π interaction between Pcs on neighbouring MNPs since Pcs are known for their π-π stacking to form aggregates [43]. The size distribution histograms show the estimates of the sizes of the spheres representing the GSH-$CoFe_2O_4$ MNPs, $CoFe_2O_4$-**1** and $CoFe_2O_4$-**2** to be 10.75 nm, 14.85 nm and 16.10 nm, respectively.

Dynamic light scattering (DLS), Fig. 6, showed an increase in size of the GSH-$CoFe_2O_4$ MNPs following conjugation to complexes **1** and **2**, Table 1. The sizes obtained for GSH-$CoFe_2O_4$ MNPs, $CoFe_2O_4$-**1** and $CoFe_2O_4$-**2** are 10.08, 14.10 and 16.95 nm respectively, similar to those obtained from TEM. It is expected that sizes from DLS would be slightly higher than those from TEM due to the interference of the dispersant into the hydrodynamic diameter, however, DLS-numbers are close to the TEM results. As observed before [44] DLS number distribution can be close to those obtained from TEM while DLS intensity distribution usually has a large difference with TEM. It was proven that the DLS-numbers show a good approximation
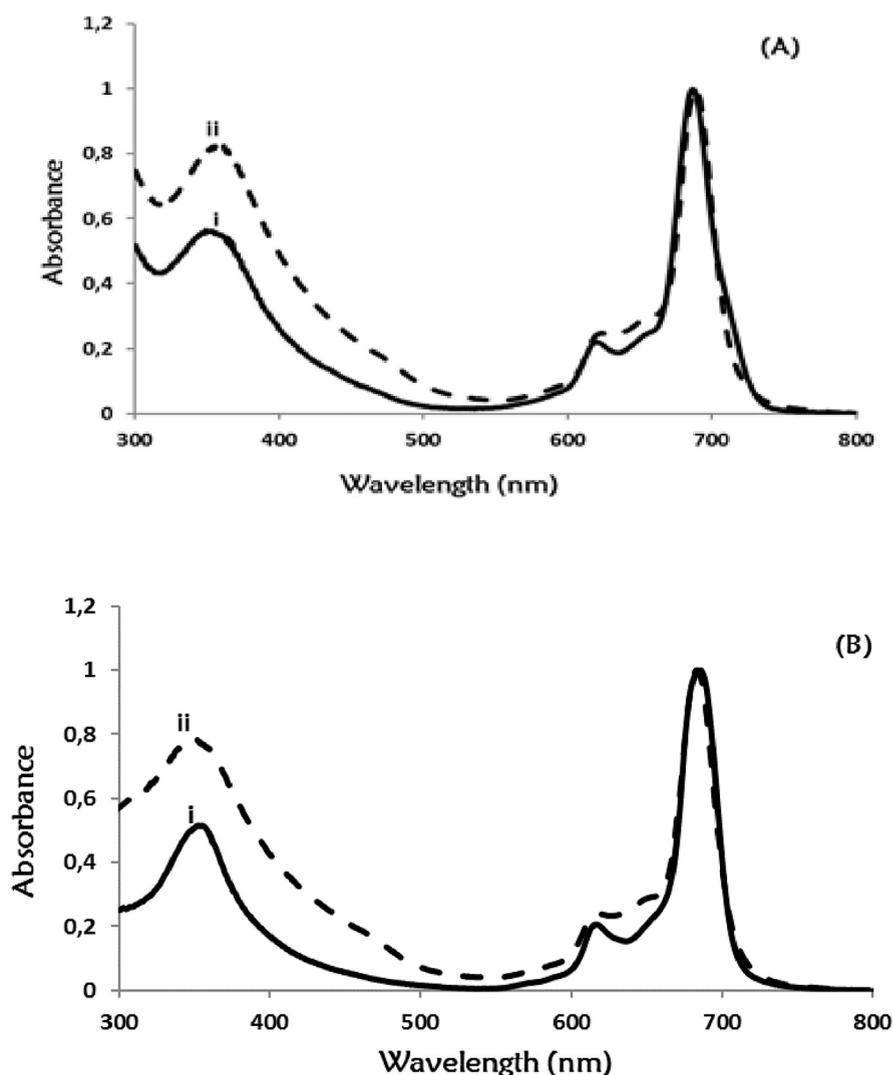
Fig. 4. Ground state absorption spectra of (A) (i) complex **1**, (ii) $CoFe_2O_4$-**1**, and (B) (i) complex **2**, (ii) $CoFe_2O_4$-**2** in DMSO.

to the size parameters obtained by TEM while DSL-intensity does not. These errors are more evident on the results of mixed samples with different sizes, where the DLS-intensity present values may be up to five times larger than TEM.

X-ray Diffraction (XRD) patterns of the compounds were analysed as shown in Fig. 7. The GSH-$CoFe_2O_4$ MNPs show characteristic peaks attributed to a cubic spinel structure with peaks at $2\theta = 29^o$, 36°, 43°, 54°, 57° and 63° corresponding to hkl Miller indices of (220), (311), (400), (422), (511) and (440), respectively [45]. Complex **1** has a broadened peak at $\sim 2\theta = 26^o$ which is typical for Pcs [46]. The $CoFe_2O_4$-**1** on the other hand has peaks corresponding to both the GSH-$CoFe_2O_4$ MNPs and complex **1**. This is an indication that the conjugate is indeed a composite of the two photocatalysts and that the GSH-$CoFe_2O_4$-NH_2
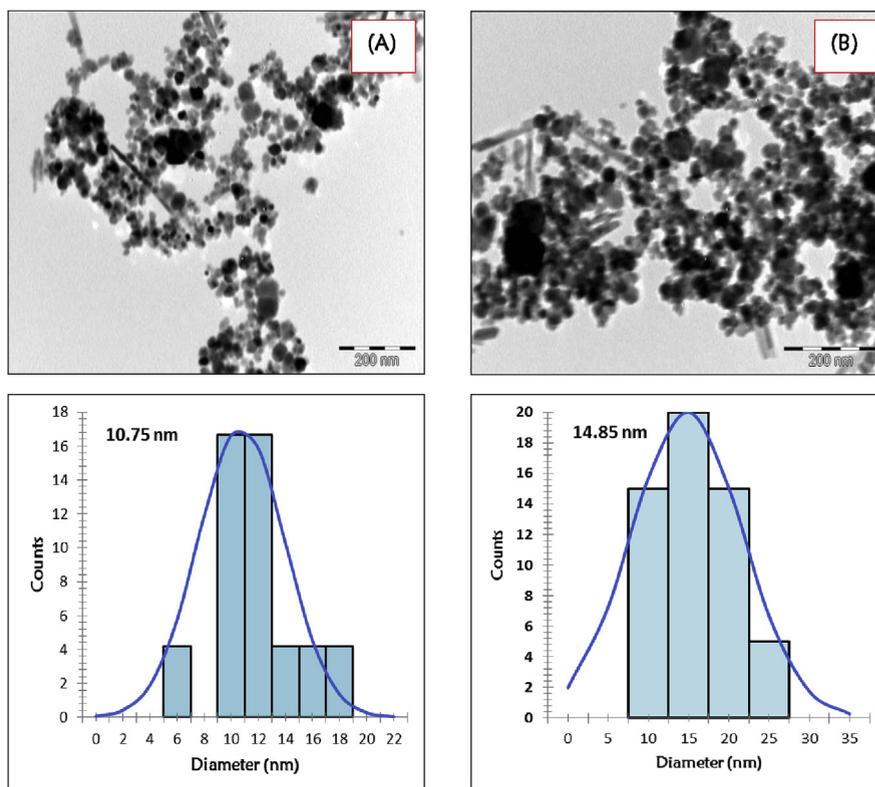
**Fig. 5.** TEM images of the (A) GSH-CoFe$_2$O$_4$ MNPs and (B) CoFe$_2$O$_4$-**1** and their respective histograms.

MNPs retain their crystallinity when conjugated to Pcs, which also retain their amorphous nature in the conjugate. Similar diffraction patterns were obtained for complex **2** and CoFe$_2$O$_4$-**2** (figure not shown).

Energy Dispersive X-ray Spectroscopy (EDX) was conducted for confirmation of the elemental composition of the MNPs, Pcs and conjugates (using the bare and functionalised CoFe$_2$O$_4$ MNPs, complex **2** and CoFe$_2$O$_4$-**2** as examples). As shown in Fig. 8, the GSH-CoFe$_2$O$_4$ have S peak which is absent in the bare CoFe$_2$O$_4$ MNPs, an indication of efficient incorporation of glutathione on the surface of the bare MNPs. Complex **2** has the expected C, N, O and Zn peaks of a Pc and its Pc-MNP conjugate (CoFe$_2$O$_4$-**2**) on the other hand has peaks from the GSH-Co-Fe$_2$O$_4$ MNPs and an additional Zn peak from complex **2**, that being an indication of pure elemental composition of the Pcs, MNPs and conjugates.

Fourier-transform infrared (FT-IR) spectroscopy was used to elucidate the structural properties of the MNPs. It was also used to confirm functionalization of the MNPs with glutathione as well as efficient covalent bond formation between the MNPs and Pc complexes, Fig. 9 (using complex **1** as an example). IR bands at 3033 cm^{-1} and 2540 cm^{-1} representing carboxylic acid O-H stretch and the S−H stretch,
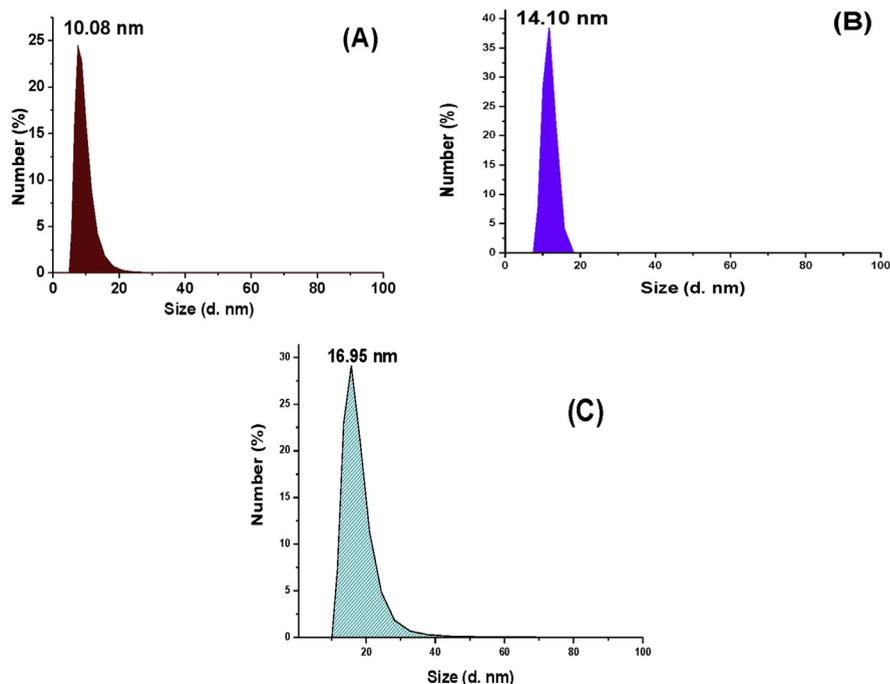
**Fig. 6.** DLS plots of (A) GSH-CoFe$_2$O$_4$, MNPs, (B) CoFe$_2$O$_4$,-**1,** and (C) CoFe$_2$O$_4$-**2**.
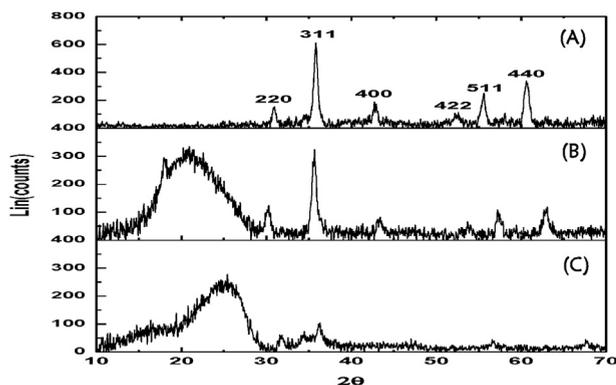
Fig. 7. X-ray diffraction patterns of (A) GSH-CoFe$_2$O$_4$ MNPs, (B) CoFe$_2$O$_4$-**1**, and (C) complex **1**.

respectively, were observed for glutathione (Fig. 9 **A(i)**). The S-H stretch diminished in the GSH-CoFe$_2$O$_4$ MNPs (Fig. 9 **A(ii)**) due to covalent interaction of the gluta-thione to the bare MNP through the thiol group. There was also an observed IR band at 1545 cm^{-1} for glutathione (Fig. 9 **A(i)**), representing the amide moieties in its chain as well as bands between $\sim$ 1000 cm^{-1} and 500 cm^{-1}, representing its C-H, C-N and C-C bonds. The bands at 444 cm^{-1} and 592 cm^{-1}, observed for GSH-CoFe$_2$O$_4$ MNPs (Fig. 9 **A(ii)**) are characteristic for metal-oxygen bonds for spinel ferrite structure [47]. They represent the octahedral metal-oxygen and tetrahe-dral metal-oxygen stretching vibrations, respectively [48]. The amide bond and car-boxylic acid O-H stretch are also maintained with bands at 1595 cm^{-1} and 3012
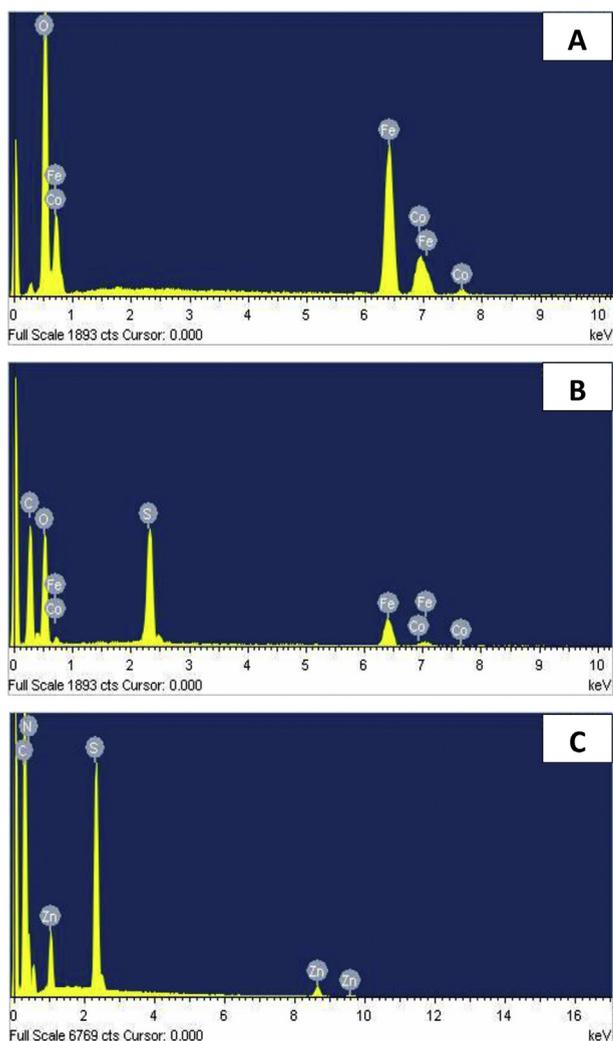
Fig. 8. EDX spectra of (A) Bare CoFe$_2$O$_4$ MNPs, (B) GSH-CoFe$_2$O$_4$ MNPs, (C) complex **2,** and (D) CoFe$_2$O$_4$-**2.**

cm^{-1}, respectively. The FT-IR spectrum of complex **1** (Fig. 9 **B(i)**) showed peaks corresponding to the N-H stretch were observed at 3185 and cm^{-1} and 3320 cm^{-1} and an N-H bend peak was observed at 1548 cm^{-1}, due to the primary amine. The carboxylic acid O-H stretch of the GSH-CoFe$_2$O$_4$ MNPs and the primary amine stretch of complex **1** are absent in their conjugate (CoFe$_2$O$_4$-**1**) instead there is an observed C-H stretch at 2951 cm^{-1}. There is also an amide peak at 1565 cm^{-1} in addition to the characteristic peaks of the spinel MNPs, this is indication of successful amide bond formation between the MNPs and Pc complexes (complex **1** in this case).
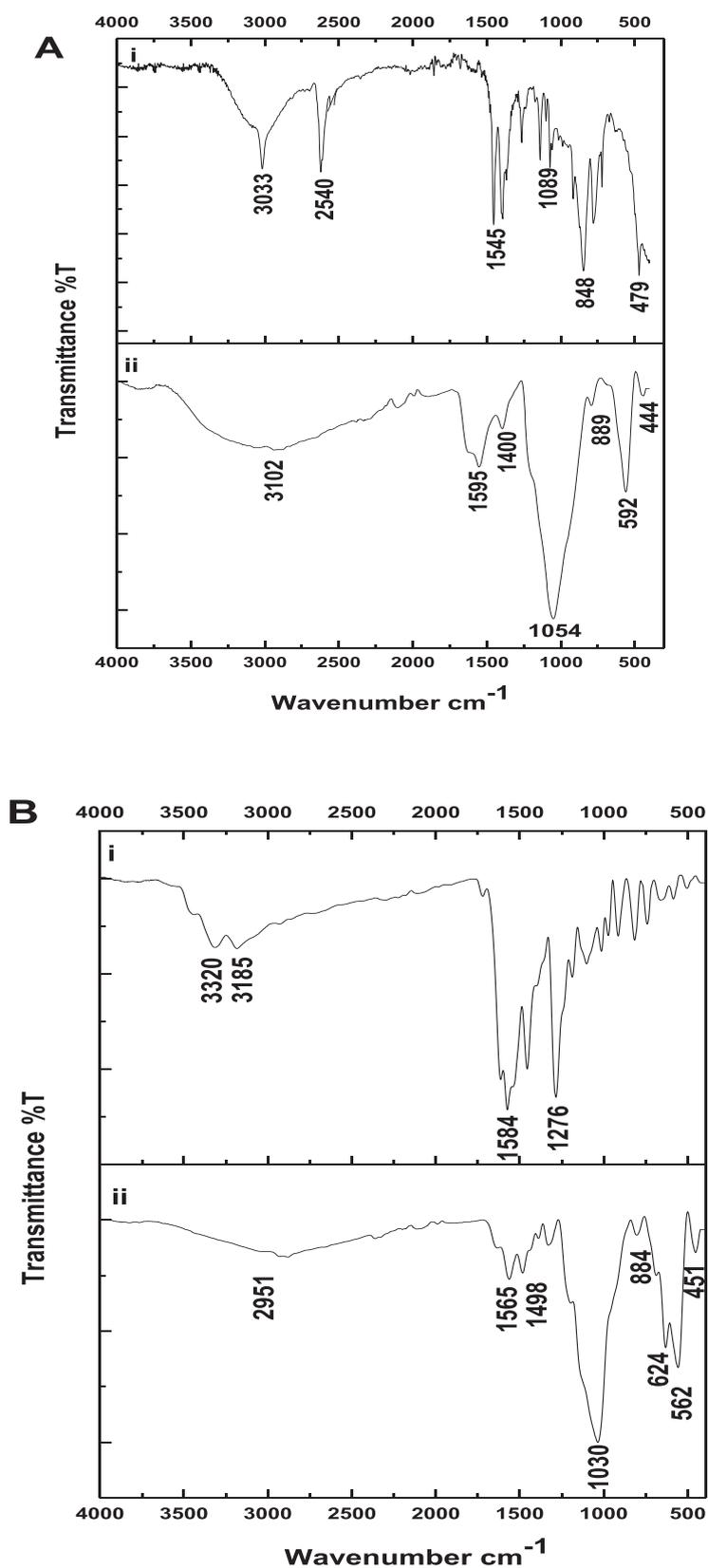
Fig. 9. FT-IR spectra of (A) (i) glutathione only, (ii) GSH-CoFe$_2$O$_4$ MNPs, (B) (i) complex **1** and (ii) CoFe$_2$O$_4$-**1.**
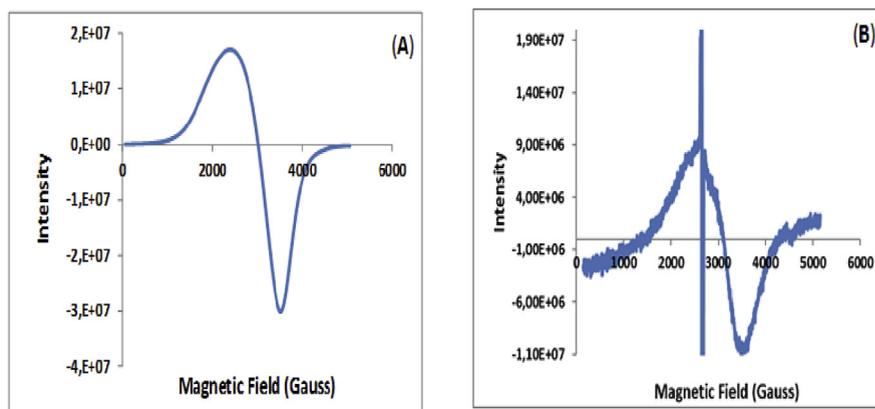
Fig. 10. EPR spectra of (A) GSH-CoFe$_2$O$_4$ MNPs and (B) CoFe$_2$O$_4$-**1.**

The EPR spectroscopy is highly sensitive to the local electronic structure, oxidation state and the vicinity of the magnetic species. EPR was used in this work to investigate the magnetic properties at high frequency due to the resonance originating from the interaction between spins and electromagnetic waves. At room temperature, the first derivative EPR spectrum (Fig. 10) of the GSH-CoFe$_2$O$_4$ MNPs shows a mixing of two lines consisting of a broad component corresponding to typical anisotropic contributions and a narrow one, which has been attributed to surface isotropic contributions [35]. This is typical for superparamagnetic resonance [35]. The position of resonance i.e. effective *g*-value was calculated to be 2.005 for the GSH-CoFe$_2$O$_4$ MNPs, a value that is typical for paramagnetic compounds [49]. Upon conjugation of the GSH-CoFe$_2$O$_4$ MNPs with the Pcs (using CoFe$_2$O$_4$-**1** as an example), there was a slight reduction in the intensity of the spectrum, suggesting that the magnetic behaviour of the MNPs slightly decreased after conjugation. There is also an observed narrow, high intensity signal with an effective g-value of 2.002 suggesting the presence of ZnPc$^{\bullet+}$ in the conjugate [50]. The obtained results are therefore an indication that the MNPs and Pc-MNP conjugates reported herein are indeed superparamagnetic and were magnetically retrieved for possible re-use.

X-ray photoelectron spectroscopy (XPS) survey scans (Fig. 11A and C) shows the expected elements for both the GSH-CoFe$_2$O$_4$ MNPs and the Pc complexes while the conjugates (CoFe$_2$O$_4$-**1** and CoFe$_2$O$_4$-**2**) have elements from their respective Pcs and GSH-CoFe$_2$O$_4$ MNPs. Although complex **1** does not have oxygen but there is an observed O1s peak. It has been reported that samples exposed to the atmosphere, whether due to adventitious contamination, oxidation or exposure to water will usually have an oxygen peak [51].

The N 1s high resolution peak for the GSH-CoFe$_2$O$_4$ MNPs was deconvoluted to yield three components at 398.3 eV, 399.5 eV, and 401.7 eV corresponding to N-C, N-H and N-C = 0, respectively (Fig. 11B(i)). The component at high binding energy (401.7 eV) is representative of the amide bond present in the glutathione
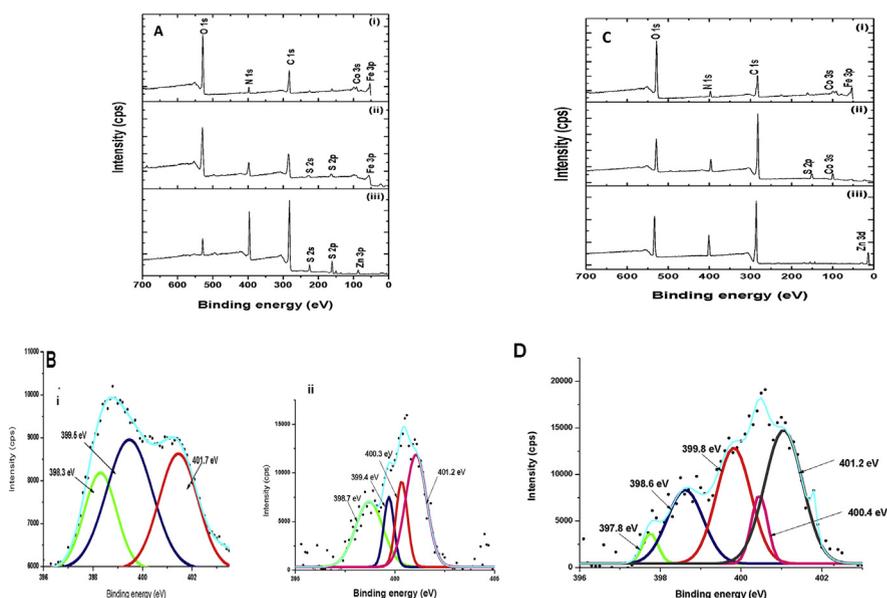
Fig. 11. (A) Wide scan XPS for (i) GSH-CoFe$_2$O$_4$ MNPs, (ii) CoFe$_2$O$_4$-**1** and (iii) complex **1**, (B) High resolution XPS (N Is) spectra for (i) GSH-CoFe$_2$O$_4$ MNP and (ii) CoFe$_2$O$_4$-**1,** (C) Wide scan XPS for (i) GSH-CoFe$_2$O$_4$ MNPs, (ii) CoFe$_2$O$_4$-**2** and (iii) complex **2**, and (D) High resolution XPS (N Is) spectra for CoFe$_2$O$_4$-**2**.

backbone. The high resolution N 1s XPS spectrum for complex **1** was deconvoluted to show two peaks [24]. The high resolution N 1s for CoFe$_2$O$_4$-**1** on the other hand was deconvoluted to four components at 398.7 eV (N=C), 399.4 eV (N-C), 400.3(N-H) and 401.2 eV (N-C=O), Fig. 11B **(ii)**. The high resolution N 1s for complex **2** was deconvoluted to show four components [17]. The high resolution N 1s for CoFe$_2$O$_4$-**2** on the other hand was deconvoluted and showed five components at 397.8eV (N=C), 398.6 eV (N), 399.8 eV (N-C), 400.4 eV (N-H) and 401.2 eV (N-C=O), Fig. 11D. The intensities of the higher binding energy components (401.2 eV) are higher at 11730 cps and 14620 cps for CoFe$_2$O$_4$-**1** and CoFe$_2$O$_4$-**2** respectively compared to 2630 cps obtained for the GSH-CoFe$_2$O$_4$ MNPs. These results suggest that there is an increase in the number of amide bonds upon conjugation of the GSH-CoFe$_2$O$_4$ MNPs with the respective Pcs. The results also show that although complex **1** which has 8 terminal amine groups, forms less covalent bonds (less intensity of the amide bond peak) than complex **2**. This could be attributed to steric hinderance due to the multiple sites of attachment and hence various ways that the complex **1** and GSH-CoFe$_2$O$_4$ MNPs can bond.

3.2. Photophysical and photochemical properties

3.2.1. Fluorescence quantum yields (Φ_F) and lifetimes (τ_F)

When Pcs are conjugated to MNPs, the latter introduces a heavy atom effect which enhances intersystem crossing (ISC) of the Pc to the triplet state and hence decreases

fluorescence. This therefore means that lower Φ_F are expected for Pc-MNP conjugates compared to their respective Pcs. As seen in Table 1, complex **1** has a Φ_F of 0.11 [24] while $CoFe_2O_4$-**1** has a Φ_F of 0.058. Complex **2** on the other hand has a Φ_F of 0.060 [26] while $CoFe_2O_4$-**2** has a Φ_F of <0.01. These results therefore show that most of the energy of the excited photosensitizer is transferred through ISC and very little is given off through fluorescence.

A fluorescence decay curve using $CoFe_2O_4$-**1** as an example is shown in Fig. 12A, where the curves show biexponential decays. This type of decay may occur for Pcs due to the formation of aggregates which are non-fluorescent, but which can quench the monomer [52]. For the Pc-MNP conjugates, the bi-exponential fluorescence lifetimes could be due to the orientation of the Pcs around the NPs [53]. The reported τ_F for complexes **1** and **2** are 2.53 and 2.79 ns, respectively [24, 26], while those for $CoFe_2O_4$-**1** and $CoFe_2O_4$-**2** are 2.29 and 2.20 ns, respectively. The shortening in τ_F corresponds to the decrease in Φ_F of the Pcs when in the presence of MNPs.
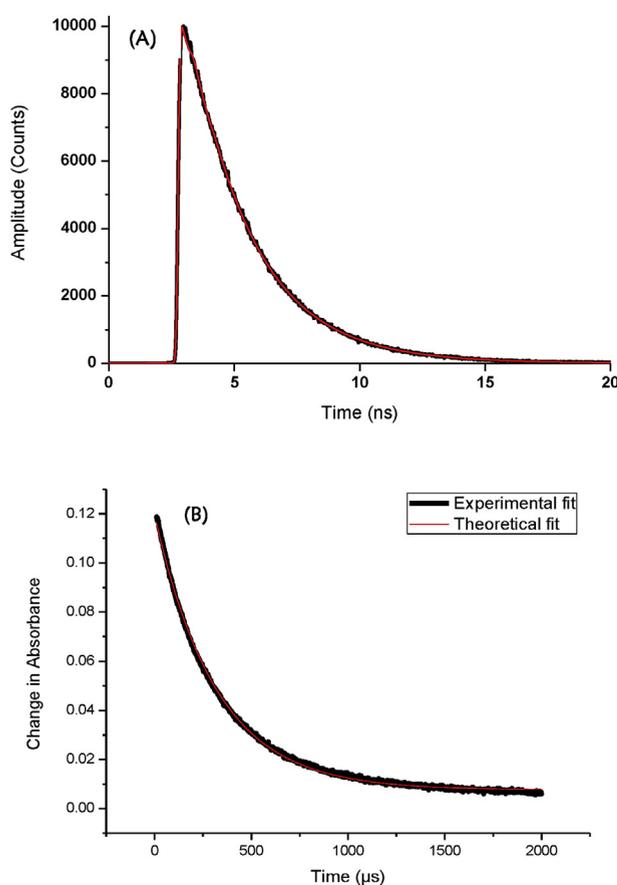
Fig. 12. (A) Fluorescence lifetime decay and (B) triplet decay curves for $CoFe_2O_4$-**1** in DMSO.

3.2.2. Triplet quantum yields (Φ_T) and lifetimes (τ_F)

A triplet decay curve of a Pc-MNP conjugate is shown in Fig. 12B (using $CoFe_2O_4$-**1** as an example). The Φ_T of complex **1** is 0.83 [24] while that of $CoFe_2O_4$-**1** was found to be 0.88, Table 1. Complex **2** has been reported to have a Φ_T of 0.51 [26] while that of $CoFe_2O_4$-**2** was found to be 0.85. The results show that when Pcs are in the presence of MNPs, there is an increase in Φ_T due to the heavy atom effect of the $CoFe_2O_4$ MNPs. The greater enhancement in the Φ_T for $CoFe_2O_4$-**2** than $CoFe_2O_4$-**1** could be due to the larger loading of Pc onto MNPs in the former. The reported τ_T for complexes **1** and **2** are 351 and 315 µs [24, 26] while $CoFe_2O_4$-**1** and $CoFe_2O_4$-**2** were found to have τ_T of 355 and 256 µs, respectively. It has been reported that when Φ_T increases, τ_T will decrease [54] as observed for the $CoFe_2O_4$-**2**. The lengthening of τ_T for the Pc in $CoFe_2O_4$-**1** could be due to it being shielded by the MNPs as observed before [17].

3.2.3. Singlet oxygen quantum yield (Φ_Δ)

In this work, the Φ_Δ values of the photocatalysts were determined using DPBF as a singlet oxygen quencher in DMSO. The decay of DPBF upon irradiation with increased time is shown in Fig. 13 wherein $CoFe_2O_4$-**1** was used as an example. No significant changes in the intensity of the Q band were observed for the period of irradiation, that being an indication of the photostability of the Pcs and their respective conjugates. DPBF did degrade though and was monitored at 417 nm. The reported Φ_Δ for complex **1** is 0.30 [24] while $CoFe_2O_4$-**1** was found to have a Φ_Δ of 0.65. Complex **2** on the other hand has a reported Φ_Δ of 0.38 [26] while $CoFe_2O_4$-**2** has a Φ_Δ of 0.62, Table 1. When conjugated to single metal Fe_3O_4 MNPs, the Φ_Δ of complex **1** was found to be 0.41 [24] compared to the 0.65 found here when GSH-$CoFe_2O_4$ MNPs are used. Thus, the conjugation of Pcs to mixed metal MNPs ($CoFe_2O_4$ MNPs in this case) enhances Φ_Δ compared to when single metal
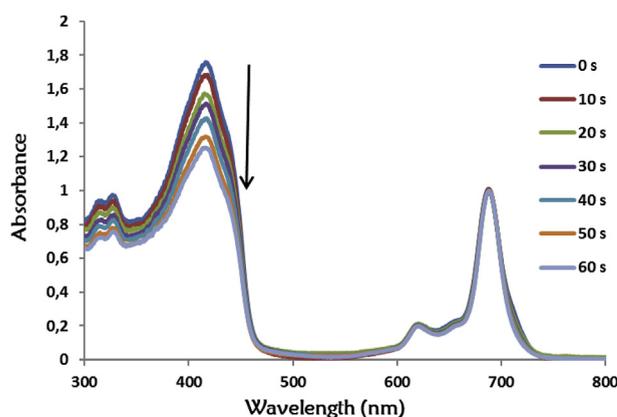

Fig. 13. Photodegradation of DPBF in the presence of $CoFe_2O_4$-**1** in DMSO with an initial concentration of DPBF = 5.9×10^{-5} molL^{-1} at 10 s irradiation intervals.

MNPs are used. This is not surprising as mixed metal MNPs have been reported to show more catalytic activity compared to their corresponding single component metal oxides [14].

3.3. Photocatalysis

3.3.1. Photodegradation of MO

Photooxidation was conducted at room temperature with pH of 2.75 because it has been reported that the photodegradation of MO is enhanced at pH values in the range 2–3 [55,56]. The photocatalysts (Pcs or their conjugates) are not soluble in water, hence they were suspended in MO solution as solids. The peak at 506 nm corresponding to the azo bond decreased in intensity with increased irradiation in the presence of $CoFe_2O_4$-**1** (used as example) while the bands below 330 nm increased in intensity, Fig. 14. The latter bands are due to the benzene rings [57, 58]. The obtained spectra therefore suggest that the benzene rings remain intact and are not degraded during the photooxidation process as observed before [57]. Since the Pc complexes used for the study are not water soluble, there is no observed Pc Q band in the degradation spectra. The color of MO was observed to also fade with irradiation time, this is because the azo bond determines the colour of the azo dyes and is very reactive usually undergoing oxidation, leading to fading of their colour [59].

The photocatalysts were applied in the degradation of five concentrations of MO with a catalyst loading of 1.0 mg/mL. The initial rates and rate constants (k_{obs}) for the photodegradation of MO increased (while the half-life decreased) with an increase in the MO concentration (Table 2). Plots for ln (C_O/C) versus irradiation time are linear (Fig. 15) confirming pseudo first order kinetics. Both conjugates
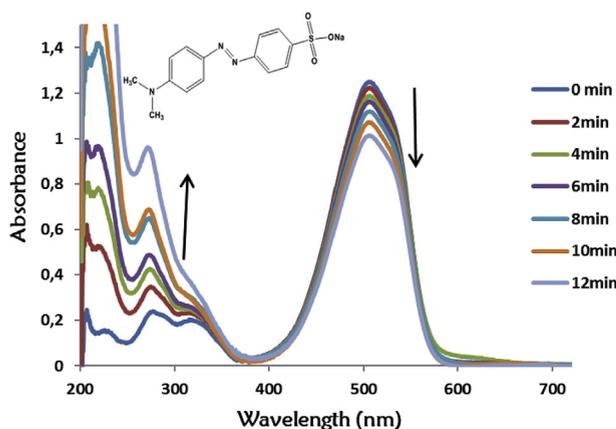
Fig. 14. Absorption spectral changes of 2.67×10^{-5} molL^{-1} MO solution during visible light photocatalysis using $CoFe_2O_4$-**1** in water with irradiation intervals of 2 min at pH 2.75. Insert = the structure of MO.

H e l i y o n

Article No~e01509

Table 2. Rates, rate constants (k_{obs}) and half-lives ($t_{1/2}$) of various initial concentrations of MO using GSH-CoFe$_2$O$_4$, complexes **1** and **2** and their respective conjugates (CoFe$_2$O$_4$-**1** and CoFe$_2$O$_4$-**2**).

| [MO] × 10^{-5} (mol L^{-1})	k_{obs} (min^{-1})					Rate (10^{-7} mol L^{-1} min^{-1})					$t_{1/2}$ (min)				
	GSH-CoFe$_2$O$_4$	1	CoFe$_2$O$_4$-1	2	CoFe$_2$O$_4$-2	GSH-CoFe$_2$O$_4$	1	CoFe$_2$O$_4$-1	2	CoFe$_2$O$_4$-2	GSH-CoFe$_2$O$_4$	1	CoFe$_2$O$_4$-1	2	CoFe$_2$O$_4$-2
3.40	0.118	0.132	0.221	0.136	0.221	40.1	44.9	75.1	46.2	75.1	5.87	3.14	3.13	5.10	3.13
2.67	0.0520	0.0606	0.106	0.0610	0.105	13.9	16.2	28.3	16.3	28.0	13.3	11.4	6.54	11.4	6.60
2.13	0.0280	0.0360	0.0629	0.0380	0.0625	5.96	7.66	13.4	8.09	13.3	24.8	19.3	11.0	18.2	11.1
1.85	0.0070	0.0100	0.0254	0.0103	0.0250	1.29	1.85	4.69	1.90	4.62	99.0	69.3	27.3	67.3	27.7
1.36	0.0010	0.0042	0.0093	0.0042	0.0094	0.130	0.570	1.26	0.570	1.27	693	165	74.5	165	73.7
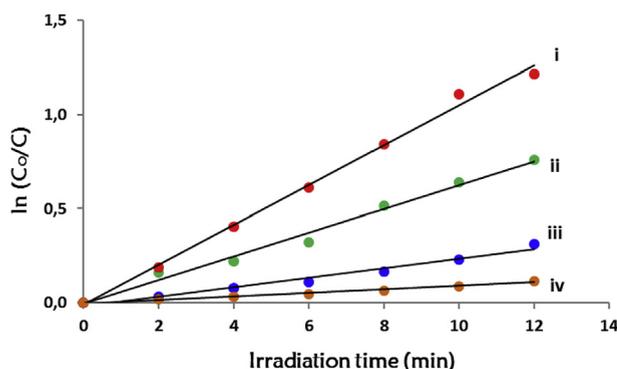
Fig. 15. Kinetics plots for degradation of MO; i. 1.85×10^{-5}, ii. 2.13×10^{-5}, iii. 2.67×10^{-5} and iv. 3.40×10^{-5} mol L^{-1} using CoFe$_2$O$_4$-**1** as a photocatalyst in water at pH 2.75.

(CoFe$_2$O$_4$-**1** and CoFe$_2$O$_4$-**2**) showed larger rates of degradation than their respective Pcs (complexes **1** and **2**). GSH-CoFe$_2$O$_4$ MNPs on the other hand were found to have the poorest photocatalytic activity. This is because, even though ferrites have been reported to have photocatalytic activity, the addition of oxidants such as H$_2$O$_2$ is often required to enhance the production of reactive oxygen species (ROS) and hence photocatalytic ability. This is because the e$^-$/h$^+$ pairs (formed on excitation) tend to recombine quickly, thereby reducing the photocatalytic ability of the ferrites [10]. When the photocatalysts were employed in the absence of irradiation and absence of oxygen (i.e. nitrogen purged solutions), only slight UV−vis spectral changes were observed, an indication that light and molecular oxygen are prerequisites in the degradation process.

3.3.2. Photoreduction of Cr (VI) to Cr (III)

UV-vis spectra for the photoreduction of Cr (VI) (Fig. 16A, using CoFe$_2$O$_4$-**1** as an example) show a decrease in two absorption peaks at 252 nm and 349 nm while there was an increase in absorption at 450 nm. The spectral changes are typical of the reduction of Cr (VI) to Cr (III) [60], wherein the latter is less toxic. The absorbance of Cr (III) was recorded (Fig. 16A (Insert)) so as to confirm that its spectrum matched that of the 450 nm peak observed in the photoreduction of Cr (VI). Photoreduction studies were conducted at a pH of 2.75 as it has been reported that the reduction of Cr (VI) is enhanced at acidic pH ranges due to the fact that the net reaction in the photo-reduction process consumes H$^+$ [60, 61, 62].

Photoreduction of Cr (VI) was not effective due to the re-oxidation of Cr (III) to Cr (VI) as explained in the introduction. In the presence of MO, substantial photoreduc-tion results were obtained. This is possibly because, when irradiated with light, MO itself absorbs the photons and gets excited. When excited, it can then transfer
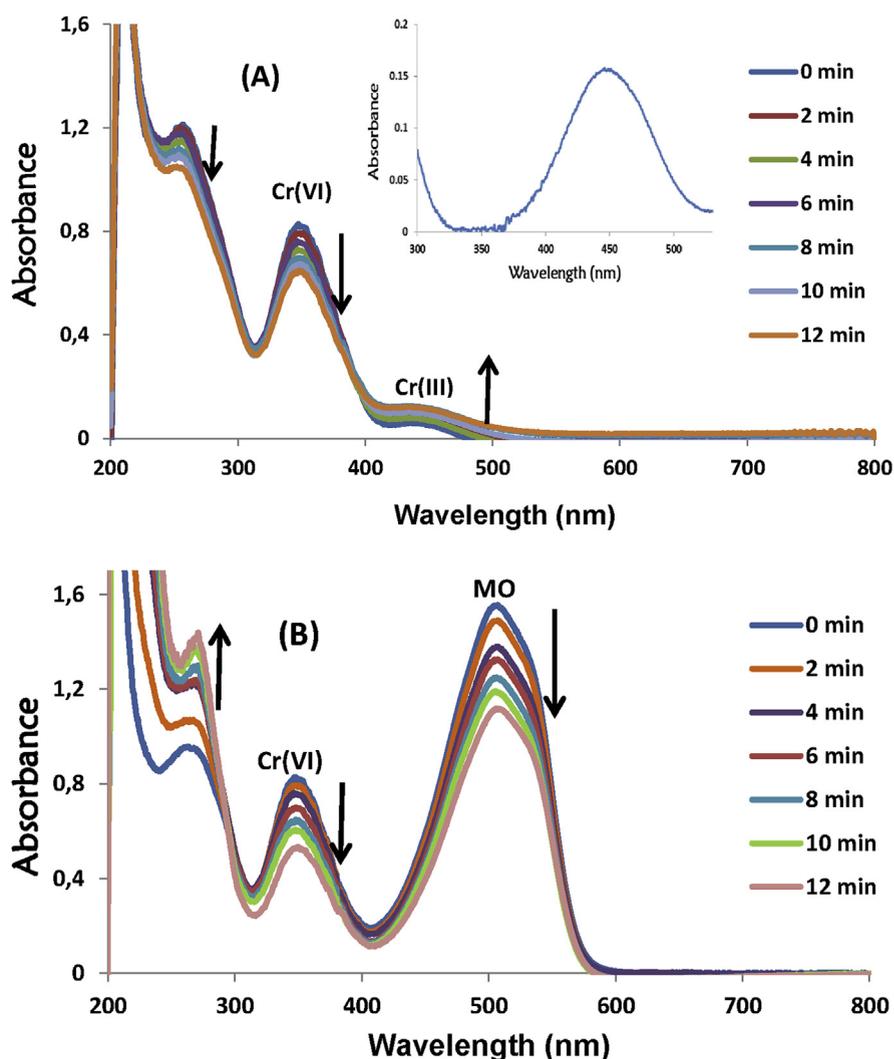
Fig. 16. Absorption spectral changes of 7.08×10^{-4} mol L^{-1} Cr (VI) solution in the absence (A) and presence (B) of 3.40×10^{-5} molL^{-1} MO, using $CoFe_2O_4$-**1** in water at 2 min interval at pH 2.75. Insert in (A) is the absorption spectrum of Cr(III).

electrons to Cr (VI) ions through the conduction band of the ferrites enhancing the reduction of Cr (VI) [63].

Spectral changes observed for Cr (VI) photoreduction in the presence of MO, are shown in Fig. 16B. There was an observed decrease of spectral peaks corresponding to both Cr (VI) (349 nm) and MO (506 nm). An increase in the band 250 nm is a result of the absorption by the oxidation products of MO as observed in Fig. 14. Due to the observed overlap between the Cr (III) and MO bands, increase in the spectral peak for Cr (III) could not be monitored so photoreduction was monitored based solely on decrease of the Cr (VI) peak.

For reasons provided above, kinetic studies for the photoreduction of Cr (VI) were conducted in the presence of 3.40×10^{-5} mol L^{-1} MO for each concentration of Cr (VI). The decrease of the peak at 349 nm was monitored and complexes **1** and **2** and their respective composites showed an increase in photoreduction efficiency (initial rates and k_{obs}) with increase in the concentration of Cr (VI), Table 3.

Plots for ln (C_O/C) versus irradiation time for the photocatalysts are linear, Fig. 17 (using CoFe$_2$O$_4$-**1** as an example), again showing pseudo-first order reaction kinetics. Complexes **1** and **2** showed lower photocatalytic activity for the reduction of Cr (VI) compared to when linked to MNPs, while GSH-CoFe$_2$O$_4$ showed the worst activity for reasons explained above.

### 3.3.3. Mechanism of simultaneous photodegradation and photoreduction

It can be elucidated that photocatalysis of Pcs in the presence of CoFe$_2$O$_4$ MNPs may occur in two ways, Fig. 18 **A** and **B**. Upon excitation with visible light, an electron−hole pair is formed in the highest occupied molecular orbital (HOMO) and lowest unoccupied molecular orbital (LUMO) of the Pc (route **1** in Fig. 18 A) [64, 65]. In ferrites, upon exposure to visible light, an electron−hole pair is formed in the conduction band (CB) and valence band (VB) respectively (route **2** in Fig. 18 A). The electrons in the LUMO of the Pc are then injected into the conduction band of CoFe$_2$O$_4$ MNPs (route **3** in Fig. 18 A). The photoelectrons can attack molecular oxygen to produce various ROS including hydroxyl radicals (·OH) (route **4** in Fig. 18 A) [19]. The photoholes possess highly oxidizing ability and can directly participate in oxidative degradation of organics or oxidise water to produce ROS including ·OH (route **5** in Fig. 18 A).

Simultaneous photooxidation and photoreduction of MO and Cr (VI), respectively have been reported before using catalysts such as cobalt ferrite meso−macroporous nanospheres, Fe(III)-grafted K$_2$Ti$_6$O$_{13}$ nanobelt and TiO$_2$ microspheres [63, 66, 67]. Interestingly, although the catalysts and reaction conditions differed, the mutual finding was that the photoreduction of Cr (VI) is enhanced in the presence of MO. This is because when Cr(VI) and MO are in a binary system, Cr(VI) acts as a strong oxidant and rapidly consumes photoelectrons at the conduction band of the MNPs thereby suppressing the charge recombination, MO on the other hand acts an oxidisable organic pollutant which consumes the photoholes at the valence band to further suppress the charge recombination. The suppressed electron−hole recombination then leads to enhanced photocatalytic efficiencies when compared to the single systems [68], as observed in this work and also enhanced by the presence of the Pcs.

A second possible mechanism (**B**) involves the intersystem crossing (ISC) of the excited Pc to the triplet state. The triplet state (^{3}Pc) has a longer lifetime (μs) than

H e l i y o n

Article No~e01509

Table 3. Rates, rate constants (k_{obs}) and half-lives ($t_{1/2}$) of various initial concentrations of Cr (VI) (in the presence of 3.40×10^{-5} molL^{-1} MO) using GSH-CoFe$_2$O$_4$, complexes **1** and **2**, CoFe$_2$O$_4$-**1** and CoFe$_2$O$_4$-**2** as photocatalysts.

[Cr (VI)] $\times 10^{-4}$ (mol L^{-1})	k_{obs} (min^{-1})					Rate (10^{-6} mol L^{-1} min^{-1})					$t_{1/2}$ (min)				
	GSH-CoFe$_2$O$_4$	1	CoFe$_2$O$_4$-1	2	CoFe$_2$O$_4$-2	GSH-CoFe$_2$O$_4$	1	CoFe$_2$O$_4$-1	2	CoFe$_2$O$_4$-2	GSH-CoFe$_2$O$_4$	1	CoFe$_2$O$_4$-1	2	CoFe$_2$O$_4$-2
9.54	0.0250	0.0309	0.103	0.0305	0.102	23.9	29.5	98.2	29.1	97.3	27.7	22.4	6.70	22.7	6.79
9.03	0.0122	0.0156	0.0674	0.0165	0.0660	11.0	14.1	60.9	14.9	59.6	56.8	44.4	10.3	42.0	10.5
8.54	0.0064	0.0084	0.0450	0.0079	0.0425	5.47	7.17	38.4	6.74	36.3	108	82.5	15.4	87.7	16.3
7.89	0.0020	0.0038	0.0292	0.0035	0.0285	1.58	3.00	2.30	2.76	2.25	346	182	23.7	198	24.3
7.08	0.0009	0.0018	0.0097	0.0019	0.0092	0.637	1.27	6.86	1.35	6.51	770	385	71.4	364	75.3
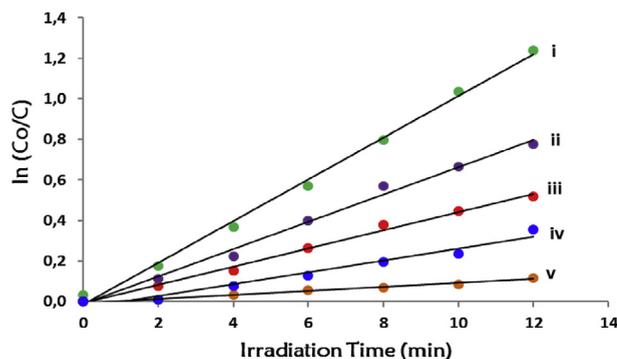
Fig. 17. First order kinetics plots for photoreduction of Cr (VI); i. 7.08×10^{-4}, ii. 7.85×10^{-4}, iii. 8.54×10^{-4}, iv. 9.03×10^{-4} and v. 9.54×10^{-4} mol L^{-1} in the presence of 3.40×10^{-5} molL^{-1} MO using CoFe$_2$O$_4$-**1** as a photocatalyst in water at pH 2.75. Study based on spectra monitored at Cr (VI) peak of 349 nm.
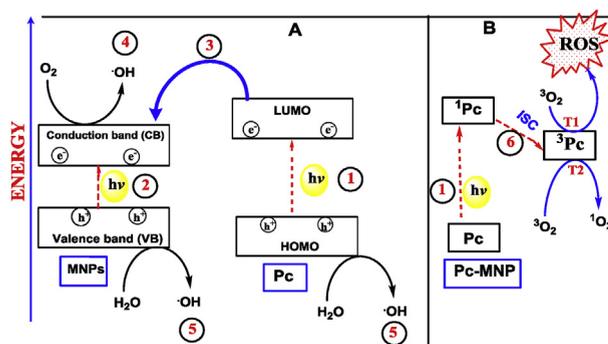
Fig. 18. The formation of ROS by photosensitization of CoFe$_2$O$_4$ MNPs and Pcs upon excitation with visible light. HOMO = highest occupied molecular orbital, LUMO = lowest unoccupied molecular orbital, ISC= intersystem crossing. T1= Type 1 and T2= Type 2.

that of the excited singlet state (^{1}Pc) (ns), enabling the Pc in the triplet excited state to react with molecular oxygen in two different ways, denoted T1 (Type 1) and T2 (Type 2) in Fig. 18 B. In the Type 1 reaction (T1), the Pc in the excited triplet state (^{3}Pc) transfers an electron to molecular oxygen (^{3}O$_2$) generating various ROS including hydroxyl radicals (·OH), peroxides (H$_2$O$_2$) and hydroxide ions (OH$^-$) [68] which have the ability to readily degrade organic pollutants. The Type 2 reaction (T2) on the other hand entails the transfer of energy from the Pc in triplet excited state (^{3}Pc) to molecular oxygen (^{3}O$_2$) thereby generating singlet oxygen (^{1}O$_2$) [8] which is itself reactive to organic pollutants.

4. Conclusion

The conjugates of complexes **1** and **2** with GSH-CoFe$_2$O$_4$ MNPs (represented as Co-Fe$_2$O$_4$-**1** and CoFe$_2$O$_4$-**2** respectively), have been successfully synthesized and

applied in a binary system for simultaneous photooxidation of MO and photoreduction of Cr (VI), using visible light. The results showed that conjugation of Pcs to GSH-CoFe$_2$O$_4$ MNPs results in improved singlet oxygen quantum yield, and enhanced photocatalytic abilities of the Pcs. The conjugates (CoFe$_2$O$_4$-**1** and CoFe$_2$O$_4$-**2**) were found to be the best photocatalyst for both the photodegradation of MO and the photoreduction of Cr (VI) relative to their respective Pcs and MNPs. The results in this work have also proven that real life applications for water purification can be devised from Pc-MNP based photocatalysts as they are effective in water containing a mixture of organic and inorganic pollutants.

Declarations

Author contribution statement

Sivuyisiwe Mapukata: Conceived and designed the experiments; Performed the experiments; Analyzed and interpreted the data; Wrote the paper.

Olawale L. Osifeko: Performed the experiments.

Tebello Nyokong: Analyzed and interpreted the data; Contributed reagents, materials, analysis tools or data; Wrote the paper.

Funding statement

Competing interest statement

The authors declare no conflict of interest.

Additional information

No additional information is available for this paper.

References

[1] T. Nyokong, in: J.H. Zagal, F. Bedioui, J.P. Dodelet (Eds.), N4-macrocyclic Metal Complexes: Electrocatalysis, Electrophotochemistry, and Biomimetic Electrocatalysis, Springer, 2006. Chpt. 7.

[2] F.S. Damos, R. de Cassia Silva Luz, A.A. Tanaka, in: J.H. Zagal, F. Bendioui (Eds.), Electrochemistry of N4 Macrocyclic Metal Complexes, Springer International Publishing, 2016, pp. 201−224.

[3] D. Lelievre, L. Bosio, J. Simon, J.J. Andre, F. Bensebaa, Dimeric substituted copper phthalocyanine liquid Crystals.Synthesis, characterization and magnetic properties, J. Am. Chem. Soc. 114 (1992) 4475−4479.

[4] M.V. Martínez-Díaz, M. Ince, T. Torres, Phthalocyanines: colorful macroheterocyclic sensitizers for dye-sensitized solar cells, Monatsh. Chem. 142 (2011) 699−707.

[5] M.A. Díaz-García, Nonlinear optical properties of phthalocyanines and related compounds, J. Porphyr. Phthalocyanines 13 (2009) 652−667.

[6] R. Bonnet, in: Chemical Aspects of Photodynamic Therapy, Gordon and Breach Science, Amsteldijk, 2000, pp. 199−222.

[7] M. Ledwaba, N. Masilela, T. Nyokong, E. Antunes, Improved photocatalytic degradation of Orange G using hybrid nanofibers, J. Nanoparticle Res. 19 (2017) 1−11.

[8] P. Modisha, T. Nyokong, Photodegradation of Orange-G using zinc octacarboxyphthalocyanine supported on Fe_3O_4 nanoparticles, J. Mol. Catal. A Chem. 380 (2013) 131−138.

[9] R. Dom, R. Subasri, K. Radha, P.H. Borse, Synthesis of solar active nanocrystalline ferrite, MFe2O4 (M: Ca, Zn, Mg)photocatalyst by microwave irradiation, Solid State Commun. 151 (2011) 470−473.

[10] E. Casbeer, V.K. Sharma, X. Li, Synthesis and photocatalytic activity of ferrites under visible light: a review, Separ. Purif. Technol. 87 (2012) 1−14.

[11] A. Arimia, L. Megatifa, L.I. Granonea, R. Dillert, D.W. Bahnemann, Visible-light photocatalytic activity of zinc ferrites, J. Photochem. Photobiol. A Chem. 366 (2018) 118−126.

[12] H. Zheng, J. Wang, S.E. Lofland, Z. Mohaddes-Ardabili, L. Ma, T. Zhao, L. Salamanca-Riba, S.R. Shinde, S.B. Ogale, F. Bai, D. Viehland, Y. Jia, D.G. Schlom, M. Wuttig, A. Roytburd, R. Ramesh, Multiferroic $BaTiO_3$-Co-Fe_2O_4 nanostructures, Science 303 (2004) 661−663.

[13] C. Borgohain, K.K. Senapati, D. Mishra, K.C. Sarma, P. Phukan, A new $CoFe_2O_4$− Cr_2O_3−SiO_2 fluorescent magnetic nanocomposite, Nanoscale 2 (2010) 2250−2256.

[14] K. Ozawa, K. Ishii, Photophysical and magnetic properties of magnetic silica gel-supported silicon phthalocyanine complexes, Phys. Chem. Chem. Phys. 11 (2009) 1019−1022.

[15] P. O'Brien, Z. Ozolins, Mechanisms in the reduction of chromium (VI) with glutathione, Inorg. Chim. Acta 161 (1989) 261−266.

[16] A. Kortenkamp, M. Casadevall, S.P. Faux, A. Jenner, R.O.J. Shayer, N. Woodbridge, P. O'Brien, A role for molecular oxygen in The formation of DNA damage during the reduction of the carcinogen chromium(VI) by glutathione, Arch. Biochem. Biophys. 329 (1996) 199−207.

[17] S. Mapukata, F. Chindeka, K.E. Sekhosana, T. Nyokong, Laser induced photodegradation of Orange G using phthalocyanine-cobalt ferrite magnetic nanoparticles conjugates electrospun in polystyrene nanofibers, J. Mol. Catal. A Chem. 439 (2017) 211−223.

[18] J.M. Meichtry, V. Rivera, Y.D. Iorio, H.B. Rodrìguez, E.S. Romàn, M.A. Grela, M.I. Litter, Photoreduction of Cr (VI) using Hydroxoaluminium-tricarboxymonoamide phthalocyanine adsorbed on TiO_2, Photochem. Photobiol. Sci. 8 (2009) 604−612.

[19] Q. Wu, J. Zhao, G. Qin, C. Wanga, X. Tong, S. Xue, Photocatalytic reduction of Cr (VI) with TiO_2 film under visible light, Appl. Catal., B 142 (2013) 142−148.

[20] J. Ma, F. Yu, L. Zhou, L. Jin, M. Yang, J. Luan, Y. Tang, H. Fan, Z. Yuan, J. Chen, Enhanced adsorptive removal of methyl orange and methylene blue from aqueous solution by alkali-activated multiwalled carbon nanotubes, ACS Appl. Mater. Interfaces 4 (2012), 5749-5460.

[21] S.S. Banerjee, M.V. Joshi, R.V. Jayaram, Removal of Cr (VI) and Hg(II) from aqueous solutions using fly ash and impregnated fly ash, Separ. Sci. Technol. 39 (2004) 1611−1629.

[22] L. Al-Khatib, F. Fraige, M. Al-Hwaiti, O. Al-Khashman, Adsorption from aqueous solution onto natural and acid activated bentonite, Am. J. Environ. Sci. 8 (2012) 510−522.

[23] R.K. Gautam, S.K. Sharma, S. Mahiya, M.C. Chattopadhyaya, in: Heavy Metals in Water: Presence, Removal and Safety, RSC, 2014, pp. 1−24. Chapter 1.

[24] O.L. Osifeko, T. Nyokong, Synthesis and physicochemical properties of zinc and indium phthalocyanines conjugated to quantum dots, gold and magnetic nanoparticles, Dyes Pigments 131 (2016) 186−200.

[25] O. Tsaryova, A. Semioshkin, D. Wohrle, V.I. Bregadze, Synthesis of new carboran-based phthalocyanines and study of their activities in the photooxidation of citronellol, J. Porphyr. Phthalocyanines 9 (2005) 268−274.

[26] R.O. Ogbodu, T. Nyokong, Effects of number of ring substituents on the physicochemical properties of zinc aminophenoxy phthalocyanine-single walled-carbon nanotube conjugate, J. Photochem. Photobiol. A Chem. 274 (2014) 83−90.

[27] D. Biswal, B.N. Peeples, C. Peeples, A.K. Pradhan, Tuning of magnetic properties in cobalt ferrite by varying Fe^{+2} and Co^{+2} molar ratios, J. Magn. Magn. Mater. 345 (2013) 1−6.

[28] R.B.N. Baig, R.S. Varma, A highly active magnetically recoverable nano ferrite-glutathione-copper (nano-FGT-Cu) catalyst for Huisgen 1,3-dipolar cycloadditions, Green Chem. 14 (2012) 625−632.

[29] K. Sanusi, J.M. Stone, T. Nyokong, Nonlinear optical behaviour of indiumphthalocyanine tethered to magnetite or silica nanoparticles, New J. Chem. 39 (2015) 1665−1677.

[30] S. Fery-Forgues, D.J. Lavabre, Are fluorescence quantum yields so tricky to measure? A demonstration using familiar stationery products, J. Chem. Educ. 76 (1999) 1260−1264.

[31] A. Ogunsipe, J.Y. Chen, T. Nyokong, Photophysical and photochemical studies of zinc (II) phthalocyanine derivatives—effects of substituents and solvents, New J. Chem. 7 (2004) 822−827.

[32] T.H. Tran-Thi, C. Desforge, C.J. Thiec, S. Gaspard, Singlet-singlet and triplet-triplet intramolecular transfer processes in a covalently linked porphyrin-phthalocyanine heterodimer, J. Phys. Chem. 93 (1989) 1226−1233.

[33] N.A. Kuznetsova, N.S. Gretsova, E.A. Kalmykova, E.A. Makarova, S.N. Dashkevich, V.M. Negrimovsky, O.L. Kaliya, E.A. Lukyanets, Relationship between the photochemical properties and structure of porphyrins and related compounds, Russ. J. Gen. Chem. 70 (2000) 133−140.

[34] C. Tshangana, T. Nyokong, The photophysical properties of multi-functional quantum dots-magnetic nanoparticles—indium octacarboxyphthalocyanine nanocomposite, J. Fluoresc. 25 (2015) 199−210.

[35] G. Vázquez-Victorio, U. Acevedo-Salas, Raúl Valenzuela, in: Ferromagnetic Resonance − Theory and Applications, IntechOpen, 2013. Chapter 7.

[36] D.O. Oluwole, T. Nyokong, Comparative photophysicochemical bahaviour of nanoconjugates of indium tetracarboxyphenoxy phthalocyanines covalently

linked to CdTe/ZnSe/ZnO quantum dots, J. Photochem. Photobiol. A Chem. 312 (2015) 34−44.

[37] P.P. Goswami, H.A. Choudhury, S. Chakma, V.S. Moholkar, Sonochemical synthesis of cobalt ferrite nanoparticles, Int. J. Chem. Eng. 2013 (2013) 1−6.

[38] H. Yang, X. Zhang, A. Tang, G. Oiu, Cobalt ferrite nanoparticles prepared by Co precipitation/mechanochemical treatment, Chem. Lett. 33 (2004) 826−827.

[39] F. Bensebaa, F. Zavaliche, P.L. Ecuyer, R.W. Cochrane, T. Veres, Microwave synthesis and characterization of. Co-ferrite nanoparticles, J. Colloid Interface Sci. 227 (2004) 104−110.

[40] M. Houshiar, F. Zebhi, Z.J. Razi, A. Alidoust, Z. Askari, Synthesis of cobalt ferrite (CoFe$_2$O$_4$) nanoparticles using combustion, coprecipitation, and precipitation methods: a comparisonstudy of size, structural, and magnetic properties, J. Magn. Magn. Mater. 371 (2014) 43−48.

[41] N.R. Panchal, R.B. Jotania, Cobalt ferrite nano particles by microemulsion route, Nanotechnol. Nanosci. 1 (2010) 17−18.

[42] L. Li, J. Zhao, N. Won, N.H. Jin, S. Kim, J.Y. Chen, Quantum dot-aluminum phthalocyanine conjugates perform photodynamic reactions to kill cancer cells via fluorescence resonance energy transfer, Nanoscale Res. Lett. 7 (2012) 386−396.

[43] M.J. Stillman, T. Nyokong, in: C.C. Leznoff, A.B.P. Lever (Eds.), Phthalocyanines: Properties and Applications, VCH Publishers, 1989. Chapter 3.

[44] T.G.F. Souza, V.S.T. Ciminelli, N.D.S. Mohallem, A comparison of TEM and DLS methods to characterize size distribution of ceramic nanoparticles, J. Phys. Conf. Ser. 733 (2016) 1−5.

[45] V. Polshettiwar, B. Baruwati, R.S. Varma, Magnetic nanoparticle supported glutathione: a conceptually sustainable organocatalyst, Chem. Commun. 0 (2009) 1837−1839.

[46] B.N. Achar, K.S. Lokesh, Studies on tetra-amine phthalocyanines, J. Organomet. Chem. 689 (2004) 2601−2605.

[47] S.N. Kane, S. Raghuvanshi, M. Satalkar, V.R. Reddy, U.P. Deshpande, T.R. Tatarchuk, F. Mazaleyrat, Synthesis, characterization and antistructure modeling of Ni nano ferrite, AIP Conf. Proc. (1953), 030089-1−030089-4.

[48] B.R. Babu, T. Tatarchuk, Elastic properties and antistructural modeling for Nickel-Zinc ferrite-aluminates, Mater. Chem. Phys. 207 (2018) 534−541.

[49] R. Díaz-Pardo, R. Valenzuela, in: Saad Osman Bashir (Ed.), Advanced Electromagnetic Waves, IntechOpen, 2015. Chapter 6.

[50] N. Karousis, J. Ortiz, K. Ohkubo, T. Hasobe, S. Fukuzumi, Á. Sastre-Santos, N. Tagmatarchis, Zinc Phthalocyanine−Graphene hybrid material for energy conversion: synthesis, characterization, photophysics and photoelectrochemical cell preparation, J. Phys. Chem. C 116 (2012) 20564−20576.

[51] H. Nohira, W. Tsai, W. Besling, E. Young, J. Petry, T. Conard, W. Vandervorst, S. De Gendt, M. Heyns, J. Maes, M. Tuominen, Characterization of ALCVD-Al_2O_3 and ZrO_2 layer using X-ray photoelectron spectroscopy, J. Non-Cryst. Solids 303 (2002) 83−87.

[52] J.A. Lacey, D. Philips, The photobleaching of disulfonated aluminium phthalocyanine in microbial systems, Photochem. Photobiol. Sci. 1 (2002) 378−383.

[53] S. Vukovic, S. Corni, B. Mennucci, Fluorescence enhancement of chromophores close to metal nanoparticles. Optimal setup revealed by the polarizable continuum model, J. Phys. Chem. C 113 (2009) 121−133.

[54] J.R. Darwent, P. Douglas, A. Harriman, G. Porter, M.C. Richoux, Metal Phthalocyanines and Porphyrins as photosensitizers for reduction of water to hydrogen, Coord. Chem. Rev. 44 (1982) 83−126.

[55] N.A. Youssef, S.A. Shaban, F.A. Ibrahim, A.S. Mahmoud, Degradation of methyl orange using Fenton catalytic reaction, Egypt, J. Petrol. 25 (2016) 317−321.

[56] S. Al-Qaradawi, S.R. Salman, Photocatalytic degradation of methyl orange as a model compound, J. Photochem. Photobiol., A 148 (2002) 161−168.

[57] R. Zugle, T. Nyokong, Zinc(II) 2,9,16,23-tetrakis[4-(N-methylpyridyloxy)] phthalocyanine anchored on an electrospun polysulfone polymer fiber: application for photosensitized conversion of methyl orange, J. Mol. Catal. A Chem. 366 (2013) 247−253.

[58] S.L. Chen, X.J. Huang, Z.K. Xu, Functionalization of cellulose nanofiber mats with phthalocyanine for decoloration of reactive dye wastewater, Cellulose 18 (2011) 1295−1303.

[59] C. Zhu, L. Wang, L. Kong, X. Yang, L. Wang, S. Zheng, F. Chen, F. Maizhi, H. Zong, Photocatalytic degradation of AZO dyes by supported TiO_2 + UV in aqueous solution, Chemosphere 41 (2000) 303−309.

[60] N. Smirnova, Y. Gnatyuk, N. Vityuk, O. Linnik, A. Eremenko, V. Vorobets, G. Kolbasov, Nanosized TiO_2 - based mixed oxide films: sol-gel synthesis,

structure, electrochemical characteristics and photocatalytic activity, Int. J. Mater. Eng. 3 (2013) 124−135.

[61] C.R. Chenthamarakshan, K. Rajeshwar, E.J. Wolfrum, Heterogeneous photocatalytic reduction of Cr (VI) in UV-irradiated titania suspensions: effect of protons, ammonium ions, and other interfacial aspects, Langmuir 16 (2000) 2715−2721.

[62] A. Idris, N. Hassan, N.S.M. Ismail, E. Misran, N.M. Yusof, A.-F. Ngomsik, A. Bee, Photocatalytic magnetic separable beads for chromium(VI) reduction, Water Res. 44 (2010), 1683−168.

[63] B. Thomas, L.K. Alexander, Enhanced synergetic effect of Cr(VI) ion removal and anionic dye degradation with superparamagnetic cobalt ferrite meso−macroporous nanospheres, Appl. Nanosci. 8 (2018) 125−135.

[64] H. You, Y. Zhao, Synthesis, characterization and visible photocatalytic performance of iron (III) tetracarboxyphthalocyanine-sensitized TiO_2 photocatalyst, J. Phys. Chem. Biophys. 6 (2016) 1000199.

[65] P. Khoza, T. Nyokong, Visible light transformation of Rhodamine 6G using tetracarbazole zinc phthalocyanine when embedded in electrospun fibers and in the presence of ZnO and Ag particles, J. Coord. Chem. 68 (2015) 1117−1131.

[66] A. Khan, U. Alam, D. Ali, M. Muneer, Visible-light induced simultaneous oxidation of methyl orange and reduction of Cr (VI) with Fe(III)-Grafted $K_2Ti_6O_{13}$ photocatalyst, Chemistry 3 (2018) 7906−7912.

[67] Y. Yang, G. Wang, Q. Deng, Dickon H.L. Ng, H. Zhao, Microwave-assisted fabrication of nanoparticulate TiO_2 Microspheres for synergistic photocatalytic removal of Cr(VI) and methyl orange, ACS Appl. Mater. Interfaces 6 (2014) 3008−3015.

[68] S.P. Stratton, D.C. Liebler, Determination of singlet oxygen-specific versus radical-mediated lipid peroxidation in photosensitized oxidation of lipid bilayers: effect of beta-carotene and alpha-tocopherol, Biochemistry 36 (1997) 12911−12920.